The Astrophysical Journal, 791:118 (16pp), 2014 August 20 doi:10.1088/0004-637X/791/2/118

ON THE DUST ENVIRONMENT OF COMET C/2012 S1 (ISON) FROM 12 AU PRE-PERIHELION TO THE END OF ITS ACTIVITY AROUND PERIHELION

F. Moreno[1], F. Pozuelos[1], F. Aceituno[1], V. Casanova[1], R. Duffard[1], J. J. López-Moreno[1], A. Molina[1,4], J. L. Ortiz[1], P. Santos-Sanz[1], A. Sota[1], A. Diepvens[2], A. S. Segundo[2], C. Bell[2], C. Labordena[2], E. Bryssinck[2], E. Cortés[2], E. Reina[2], F. García[2], F. Gómez[2], F. Limón[2], F. Soldán[2], F. Tifner[2], G. Muler[2], I. Almendros[2], J. Aledo[2], J. Bel[2], J. Carrillo[2], J. Castellano[2], J. Curto[2], J. Gaitan[2], J. L. Salto[2], J. Lopesino[2], J. Lozano[2], J. F. Hernández[2], J. J. González[2], J. L. Martín[2], J. M. Aymamí[2], J. M. Bosch[2], J. M. Fernández[2], J. R. Vidal[2], L. Montoro[2], L. Tremosa[2], M. Campas[2], O. Canales[2], P. J. Dekelver[2], R. Benavides[2], R. Naves[2], R. Castillo[2], T. Climent[2], T. Cupillari[2], and P. Yanamandra-Fisher[3]

[1] Instituto de Astrofísica de Andalucía, CSIC, Glorieta de la Astronomía s/n, E-18008 Granada, Spain
[2] Amateur Astronomical Association Cometas-Obs
[3] Space Science Institute, Boulder, CO 80301, USA
Received 2014 June 3; accepted 2014 July 2; published 2014 August 5

ABSTRACT

A Monte Carlo dust tail model has been applied to extract the dust environment parameters of the comet C/2012 S1 (ISON) from both Earth-based and *SOHO* LASCO C3 observations, performed from about six astronomical units (AU) inbound, to just after perihelion passage, when only a small portion of the original comet nucleus has survived in the form of a cloud of tiny particles. The early Afρ and image data are consistent with particle ejection from an extended active area located at latitudes 35°N to 90°N (for a prograde rotating nucleus), with the spin axis having a large obliquity ($I \sim 70°$). This configuration nicely fits the early images and Afρ data until 3.9 AU inbound, when the emission should become isotropic in order to fit the data. The analysis of LASCO images reveals that, assuming an original nucleus of $R_N = 500$ m with $\rho = 1000$ kg m^{-3}, at least half of its mass was vaporized when the comet was at about 17 $R_\odot$ inbound. We conclude that at that time the nucleus suffered a cataclysmic fragmentation releasing a huge amount of material of 2.3 $\times 10^{11}$ kg, equivalent to a sphere of 380 m in radius with density 1000 kg m^{-3}. The surviving material after perihelion passage consists of very small dust particles of 0.1–50 μm in radius with a total mass of just 6.7×10^8 kg.

Key words: comets: general – comets: individual (C/2012 S1 (ISON)) – methods: numerical – Oort Cloud

Online-only material: color figures

1. INTRODUCTION

The comet C/2012 S1 (ISON, comet ISON hereafter) was discovered by Nevski & Novichonok (2012) as a diffuse object of 8″ coma on September 21.06 UT with a 0.4 m reflector of the International Scientific Optical Network (ISON) near Kislovodsk, Russia. Just after its discovery, it soon attracted attention as an Oort cloud comet with a very short perihelion distance of just 2.7 $R_\odot$ ($R_\odot$ = solar radius, 6.955×10^8 m).

At the time of discovery, ISON was at 6.3 AU from the Sun, at a visual magnitude around 19. Given its level of activity at such a large distance and its predicted extreme proximity to the Sun at perihelion, it was expected to become a very bright target for Earth observers, becoming even brighter than the full moon. However, at around 4.2 AU inbound, the comet started to show an unexpected decrease in activity compared to its original tendency that led to a visual magnitude higher than the visual limit when it started to approach perihelion at 1–0.7 AU. After a quiescent period, the comet then experienced a strong outburst of activity at ~0.65 AU, in which the HCN and OH production rates increased substantially, by more than an order of magnitude, over 48 hr (Biver at al. 2013; Opitom et al. 2013; Agúndez et al. 2014). On November 20, the comet was too close to the Sun for Earth-based observers, but it entered the field of view of the *Solar Terrestrial Relations Observatory* spacecraft at a heliocentric distance of 0.43 AU, apparently undisrupted, clearly displaying both dust and ion tails. Later on, on November 27, the comet entered the *Solar and Heliospheric Observatory* (*SOHO*) Large Angle and Spectrometric Coronagraph Experiment (LASCO) field of view, at a distance of 0.15 AU, showing two distinct tails, one northern component consisting of an intense narrow spike, and a much broader and diffuse southern branch. Late on November 27 and during the first half of November 28, the comet head displayed strong saturation effects in the *SOHO* LASCO C3 camera, possibly associated with either disruption of the nucleus (by tidal forces or thermal stress) and/or profuse vaporization of dust particles due to high temperatures. The *SOHO* LASCO C3 camera images for dates later than November 28 14:00 UT did not show an apparent nucleus. When the comet emerged from the C2 and C3 coronagraphs it displayed a bilobed tail, with some dust in between, which weakened very fast and almost disappeared when the comet finally left the C3 field of view on December 1.

In this paper, we analyze dust tail images of the comet taken from several observatories, and combine them with Afρ data obtained by the amateur association *Cometas-Obs*. We also analyze publicly available pre- and post-perihelion *SOHO* LASCO C3 images in order to have a complete view of the evolution of the dust until the comet was finally disrupted. To perform the analysis and to derive the dust parameters, we use our Monte Carlo dust tail code as in previous papers (e.g., Moreno et al. 2012, 2013).

[4] Also at Facultad de Ciencias, Universidad de Granada, Campus Universitario Fuentenueva, Calle Fuente Nueva, s/n, E-18001 Granada, Spain.

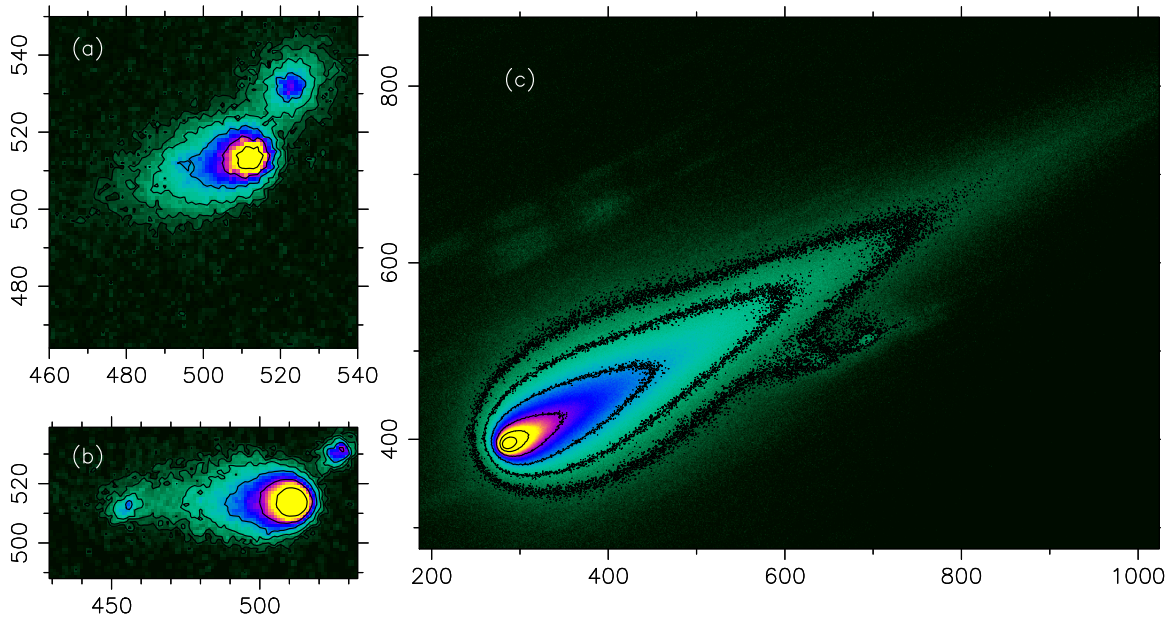

Figure 1. Panels (a) and (b): images of the comet ISON obtained at the 1.52 m telescope of the Observatorio de Sierra Nevada on 2013 February 14 and May 1, respectively. Panel (c): image obtained on 2013 October 10 with a CCD attached to the 1.23 m telescope at the Calar Alto Observatory. In all panels, north is up, and east is to the left. For more details, see Table 1.

(A color version of this figure is available in the online journal.)

Table 1
Log of the Image Observations

Date (UT)	r_h (AU)	Δ (AU)	PsAng (°)	Phase (°)	Obs/Telescope	Filter	Scale (arcsec pixel^{-1})
2013 Feb 14.04	4.784	4.008	106.433	8.01	OSN 1.52 m	Red	0.46
2013 May 01.86	3.887	4.326	90.206	12.70	OSN 1.52 m	Red	0.46
2013 Oct 06.21	1.551	1.996	291.832	29.47	OSN 1.52 m	Red	0.46
2013 Oct 10.22	1.472	1.876	292.131	31.89	CAHA 1.23 m	Red	0.50
2013 Nov 06.23	0.866	1.091	293.772	59.57	OSN 1.52 m	Red	0.46
2013 Nov 13.20	0.674	0.937	292.274	73.74	CAHA 2.2 m-CAFOS	Red	0.53
2013 Nov 15.24	0.613	0.904	291.202	78.84	OSN 0.90 m	Red	0.387
2013 Nov 28.02	0.081	0.960	251.896	106.71	*SOHO* LASCO C3	Clear	56.25
2013 Nov 28.07	0.077	0.962	250.817	106.11	*SOHO* LASCO C3	DeepRed	56.25
2013 Nov 28.62	0.026	0.991	221.337	80.19	*SOHO* LASCO C3	DeepRed	56.25
2013 Nov 28.63	0.025	0.991	219.657	78.52	*SOHO* LASCO C3	Clear	56.25
2013 Nov 29.26	0.057	0.956	11.574	120.65	*SOHO* LASCO C3	Clear	56.25
2013 Nov 29.28	0.059	0.955	10.705	121.12	*SOHO* LASCO C3	DeepRed	56.25
2013 Nov 30.21	0.128	0.902	351.353	127.80	*SOHO* LASCO C3	Clear	56.25

2. THE OBSERVATIONS

Our ground-based image data set was acquired at several telescopes from different observatories. Unless otherwise noted, all observations refer to CCD images taken through red Johnson–Cousins filters. We used the 1.52 m and 0.9 m telescopes at the Observatorio de Sierra Nevada, and the 1.23 m and 2.2 m telescopes at the Calar Alto Observatory Spain. In addition, we used several images from the *SOHO* LASCO C3 coronagraph when the comet was near perihelion. A summary of all the image observations is given in Table 1, where we provide information about the circumstances, as well as some technical aspects, of the observations. The ground-based data reduction was accomplished by standard procedures: bias subtraction and flat fielding was performed for each image, and then the frames were calibrated using the available stars on the field of view in combination with the USNO.B1.0 catalog. A median stack of the available images was then performed. The photometric calibration errors amount to ±0.3 mag. The spatial orientation of the images was also checked with the background star positions. A selection of those images are shown in Figures 1 and 2 for various epochs. Panels (a) and (b) of Figure 1 display the earliest images collected on 2013 February 14 and May 1, at 4.78 and 3.89 AU inbound, while Panel (c) displays the comet much closer to perihelion on 2013 October 10 at 1.55 AU. Figure 2 shows the comet at much shorter heliocentric distances, at 0.67 and 0.61 AU, just before and after an outburst of activity reported to occur during the earliest hours of November 14. These images display both dust and ion tails. The November 15 image is shown separately in Figure 3, after being enhanced by a Larson–Sekanina rotational filter, where wing-like features seem to emerge from the comet nucleus. This was interpreted by some authors as an indication of the fragmentation process (e.g., Boehnhardt et al. 2013).

As stated in the Introduction, we also analyzed *SOHO* LASCO C3 images in order to obtain complete coverage of the evolution of the dust around perihelion. *SOHO* continuously observes the Sun from Lagrangian point L1 (Domingo et al. 1995).

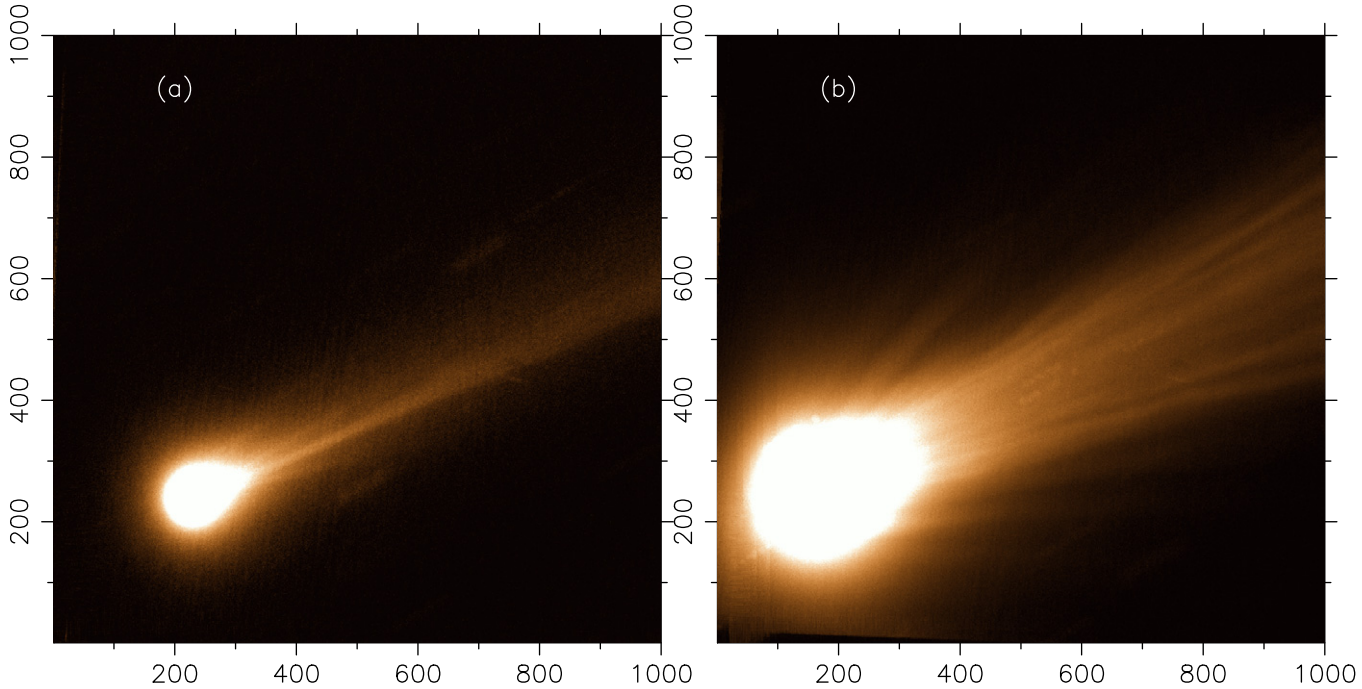

Figure 2. Panel (a): image of the comet ISON obtained on 2013 November 13 using CAFOS at the 2.2 m telescope of the Calar Alto Observatory. Panel (b): image obtained on 2013 November 15 at the 0.90 m telescope at the Sierra Nevada Observatory. In both panels, north is up, and east is to the left. More details on the images are given in Table 1.

(A color version of this figure is available in the online journal.)

For our purposes, we used pre- and post-perihelion "level-0.5" FITS images. We reduced both the DeepRed filter (at three epochs) and the Clear filter (at four epochs) images, as detailed in Table 1. The Clear filter images are mostly dominated by sodium emission (Knight et al. 2010; Knight & Battams 2014). Among the mechanisms proposed to explain the presence of alkali atom emission from comets is the evaporation of small grains (Wilson et al. 1998; Watanabe et al. 2003; Fulle et al. 2013). While other mechanisms might also play a role, this mechanism is likely operating on ISON near perihelion. Therefore, these Clear filter images are tracing cometary dust features. On the other hand, we assume that the DeepRed images are giving information on light scattered by cometary dust only. This filter bandpass (Morrill et al. 2006) is placed well outside the strong Na emission lines and the much weaker Li line at 6707.78 Å. The contamination by the weak K lines at 7664.90 and 7698.96 Å will be neglected. A quantitative estimate of the possible (small) contamination of these lines on the scattered dust flux is beyond the scope of this paper.

To perform the reduction of the *SOHO* LASCO C3 images, we built a background image by generating a median stack combining the Clear filter and DeepRed images taken at different times, so that all the background stars and the comet itself vanished, leaving a background image only. The spatial scale and rotation angle of the images with respect to the celestial north were found by fitting the stars' positions in the images to the stars in the *Hipparcos* catalog. An example of those fits for the two pre-perihelion Clear filter reduced images is given in Figure 4. This resulted in a spatial scale of $56\farcs25$ pixel^{-1}, in perfect agreement with the results of Morrill et al. (2006). Owing to the fact that the nucleus is at least partially vaporized during the observations, the position of the nucleus cannot be associated with the comet optocenter, as it is commonly done for cometary images. Instead, we located its theoretical position by using the JPL Ephemeris at the Horizons web page, taking into account that the images were taken from the location of the *SOHO* spacecraft. The position of the nucleus is displayed in the Clear images of Figure 4. Then, while the nucleus is inside the cloud of particles pre-perihelion, it is significantly away from the brightest pixel in the image in the two post-perihelion images. This fact implies that the activity (sublimation and/or refractory material vaporization) has ceased post-perihelion, which will be confirmed in the modeling procedure.

The absolute calibration was performed by using the final LASCO C3 calibration factors from Table IV of Morrill et al. (2006) for the DeepRed and Clear filters. The reduced Clear and DeepRed filter images are displayed in Figures 4 and 5. It is interesting to see the conspicuous spike along the northern part of the broader tail that is only seen in the two pre-perihelion Clear filter images. This spike is not seen at red wavelengths, possibly because it is under the detection threshold. Regarding the post-perihelion images, both the Clear and DeepRed images show two distinct tails with some material in between, one to the northeast, linked mostly to particle fragmentation near perihelion passage, as we will show in the modeling, and another to the southeast, associated with the remaining material ejected pre-perihelion.

In addition to the images, we also take into account the Afρ data provided by the amateur astronomical association *Cometas-Obs*. These data come from many observers, from several countries, mostly in Spain. These data are *R*-band Afρ data and all of them refer to a $\rho = 10^4$ km aperture radius. This data set is of great value, as they provide an almost continuous coverage of the comet dust evolution, which is very useful for retrieving dust properties from our the Monte Carlo modeling, as we will show below. Figure 6 shows the raw Afρ data as a

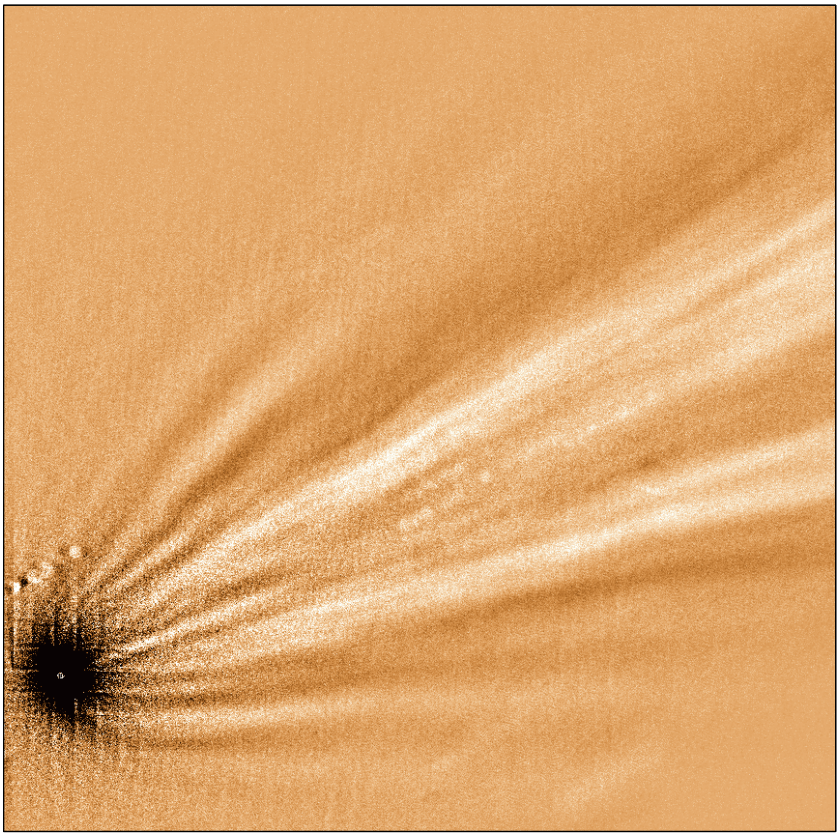

Figure 3. Larson–Sekanina filtered image of the comet ISON on 2013 November 15 (see Figure 2). North is up, and east is to the left.
(A color version of this figure is available in the online journal.)

function of time, in days related to perihelion passage (asterisks). The data begin just after discovery, shows a gap while the comet was behind the Sun in 2013 June, July, and part of August, and then span the remaining pre-perihelion branch until just 10 days before perihelion date, when the comet was again too close to the Sun. In this graph, the variation of the phase angle of the comet versus time is also shown. It is seen that the relative maximum around 320 days before perihelion is, at least partially, produced by a backscattering enhancement because of the excellent correlation of Afρ with the phase angle. In a first approximation, we corrected for this effect by assuming a linear phase coefficient of $\kappa = 0.03$ mag deg^{-1}, which is within the range of estimates of κ for other comets (e.g., Meech & Jewitt 1987). Then, for phase angles $\alpha \leqslant 30^{\circ}$, we corrected the Af$\rho$ values by the factor $10^{\kappa(30-\alpha)/2.5}$. This correcting factor was also applied to the images for which $\alpha \leqslant 30^{\circ}$. Although less pronounced, the maximum at -320 days still remains, but we did not make further corrections because we cannot be completely sure that an outburst of activity is also contributing.

3. THE MODEL

The interpretation of the images and the Afρ data is based on our Monte Carlo dust tail analysis code, which has been described previously in several papers (e.g., Moreno et al. 2012, 2013). The code is a forward model that produces synthetic dust tail images for a given observing date taking into account a set input parameters related to the dust parameters: differential size distribution, ejection velocities, and dust loss rates as a function of the heliocentric distance. In addition, the density ρ_p and the geometric albedo p_v of the dust grains must be specified. We adopt $\rho_p = 1000$ kg m^{-3}. The scattering properties of aspherical grains of a wide range of sizes, like those ejected from cometary nuclei, are very tedious to calculate using the available light scattering codes (e.g., the Discrete Dipole Approximation by Draine & Flatau 1994), mainly because of the long CPU time and huge memory needed for grains larger than the wavelength of the incident light, even for large computers. In consequence, we consider spherical dust grains, for which Mie theory gives an exact computation of the phase matrix at a given wavelength and refractive index. For a refractive index of $m = 1.88 + 0.71\,i$, which corresponds to glassy carbon, we obtain $p_v = 0.04$ at red wavelengths for grains having a radius $r \geqslant \lambda$. The main problem we face with this approximation is that the phase function is completely flat at backscattering, so that the backscattering enhancement cannot be modeled properly. This is why we resort to correct the data affected by the backscattering enhancement by the method described in the previous section.

From Mie theory, we can also obtain the radiation pressure coefficient $Q_{\rm pr}$, which turns out to be $Q_{\rm pr} \approx 1$ for $r \geqslant \lambda$. The ratio of solar radiation pressure to solar gravity force exerted on the grains can be computed as $\beta = C\,Q_{\rm pr}(2\rho_p r)^{-1}$, where $C = 1.19\ 10^{-3}$ kg m^{-2}. Neglecting cometary gravity, which is a reasonable assumption for nucleus sizes of the order of $R_N \sim 1$ km, like ISON, the grains move in Keplerian orbits around the Sun. The trajectory of the grains will be a function of the terminal velocities and the β parameter. The final position of the ejected grains on the photographic plane for a given observation date and their contribution to the tail brightness are computed by the Monte Carlo code.

The model can deal with the characteristics of the emission pattern. Adopting a spherical nucleus, it is possible to specify its rotation parameters (rotation period and orientation of the

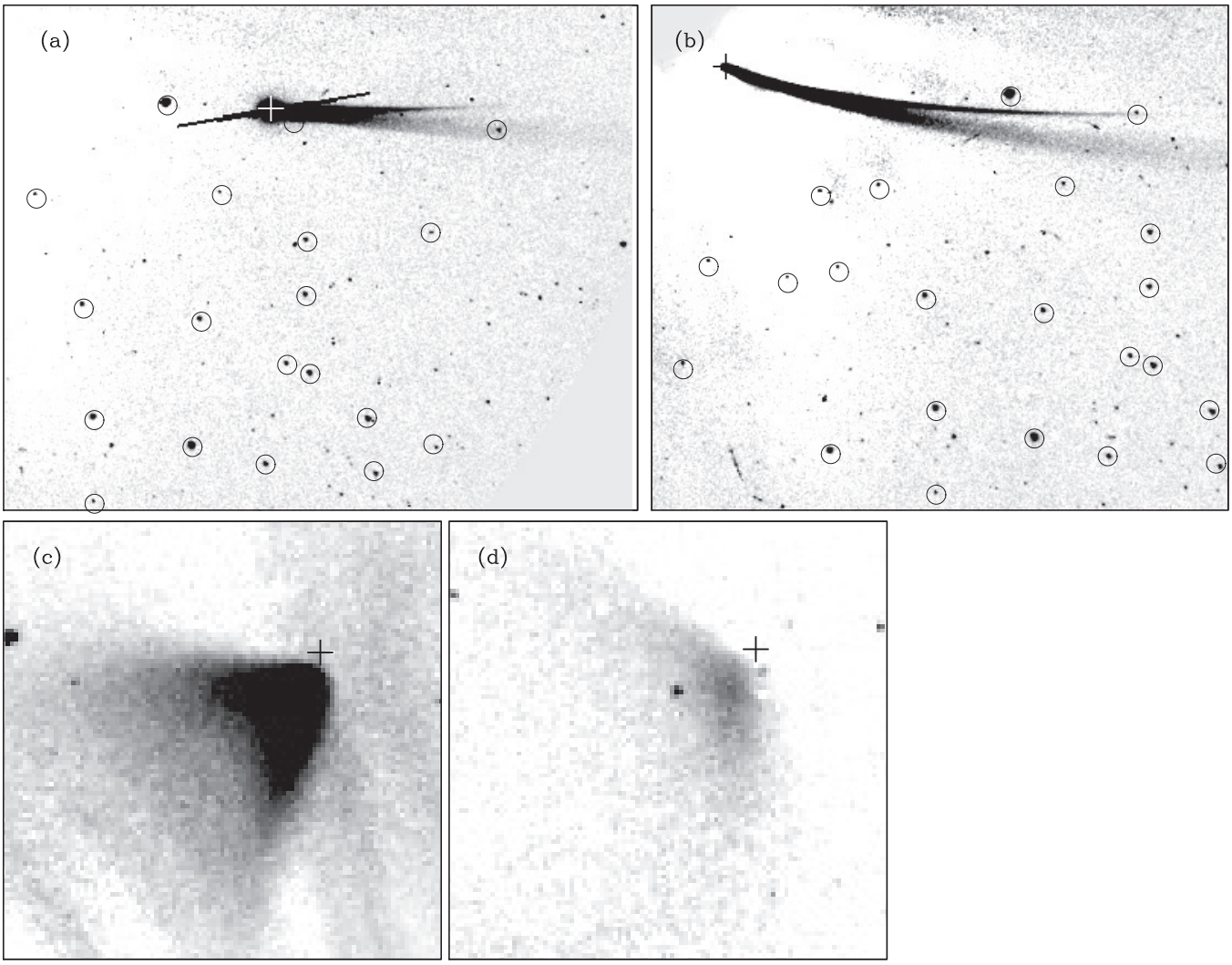

Figure 4. Reduced images of the comet ISON obtained through the Clear filter of the LASCO C3 coronagraph on the *SOHO* satellite. The dates are 2013 November 28.02 (a), 28.63 (b), 29.26 (c), and 30.21 (d). Panels (a) and (b) are pre-perihelion, and panels (c) and (d) are post-perihelion images. The crosses mark the nucleus position, according to the JPL-Horizons ephemeris. The encircled stars in panels (a) and (b) illustrate the fits to the *Hipparcos* catalog. In all panels, north is up, and east is to the left.

spin axis), and to set some active area(s) on its surface. The orientation of the spin axis is specified by the obliquity I, and the argument of the subsolar meridian at perihelion Φ (for a definition of those angles, see, e.g., Sekanina 1981). Owing to the large number of free parameters, we only resort to that anisotropic ejection model when we cannot find an acceptable fit for isotropic or hemispherical emission models.

The terminal velocity of the ejected grains is parameterized according to the expression $v(\beta, t) = v_1(t)\beta^{1/2}$. This formula has previously been used in other well-known models such as Fulle (1989), and separates the time and size dependencies of the velocity. The size dependence is appropriate to gas drag by the ice sublimation processes. The ejection velocities are parameterized as a three-dimensional vector whose components are directed outward in the direction of the comet radius vector (u_R), perpendicular to u_R, contained in the orbital plane, and in the opposite sense of the comet motion (u_θ), and normal to the orbital plane directed to the north pole of the orbit (u_z). These components must be calculated as a function of the active area coordinates and the angles I and Φ (Sekanina 1981).

To model the dust tail observations at different epochs, we start from a specific choice of input parameters as follows. The differential size distribution function is set in the interval 10^{-5} cm to an upper size limited by the escape velocity, given by $v_{\rm esc} = \sqrt{2GM/R}$, where R is the distance to the nucleus center of mass. We adopt $R = 20\ R_N$, the distance at which the gas drag becomes negligible. Then, for a spherical nucleus of $R_N = 500$ m, which would agree with the reported nucleus size by Combi et al. (2014), $0.3 < R_N < 1.3$ km, and a bulk nuclear density of $\rho_N = 1000$ kg m^{-3}, the nucleus mass is 5.2 10^{11} kg, and the escape velocity becomes 0.08 m s^{-1}. The differential size distribution function is initially assumed constant with the heliocentric distance and having a power index of -3.5, which is within the range estimated for many comets. The onset time of cometary activity was set at 12 AU. At the first pre-discovery observation by Pan-STARRS, on 2011 September 30 (see the available magnitude data for ISON in the Minor Planet Center database), the comet was at 9.4 AU, so that we placed a safe onset time earlier, as the comet might already be active at the time of the first observation. In any case, this date was tested in the modeling procedure. With these parameters, we attempted first to fit our earliest images on 2013 February 14 and May 2, in combination with the first part of Afρ data from -430 to -200 days to perihelion, and then the rest of images and Afρ

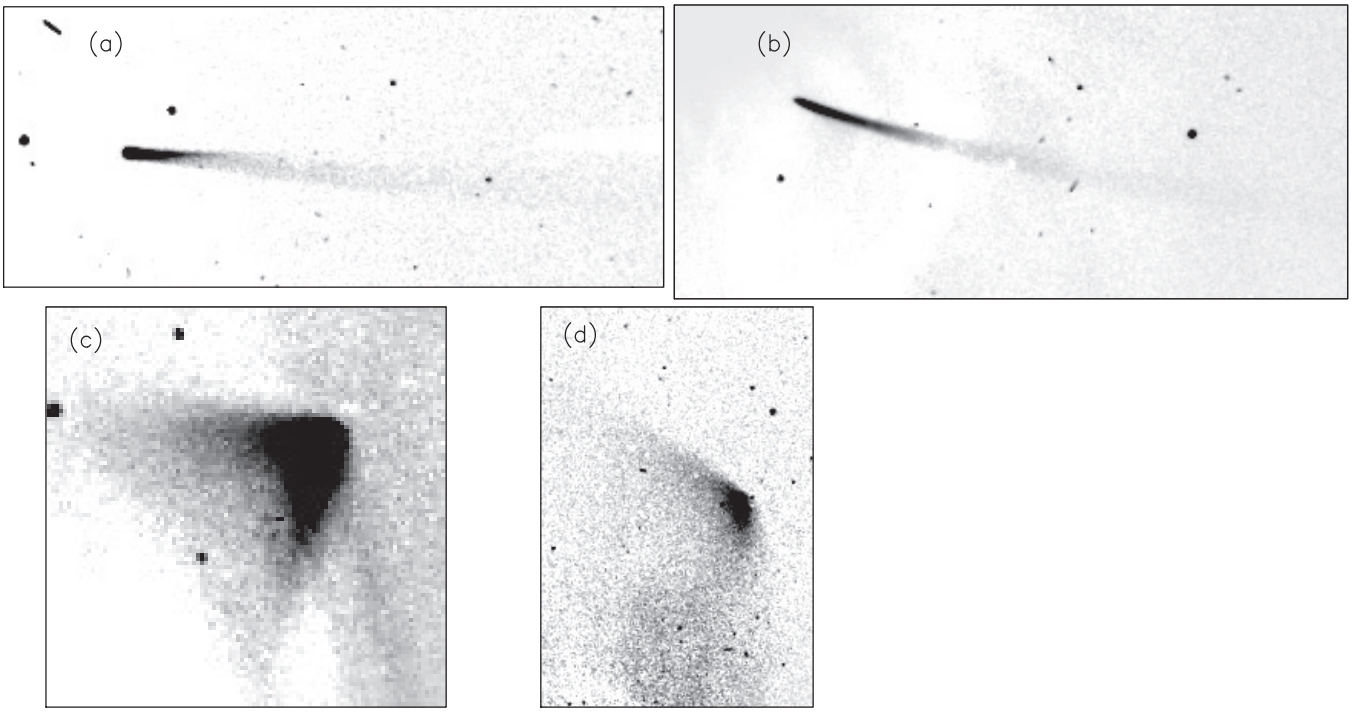

Figure 5. Panels (a), (b), and (c): reduced images of the comet ISON obtained through the DeepRed filter of the LASCO C3 coronagraph on the *SOHO* satellite. The dates are 2013 November 28.07 (a), 28.62 (b), and 29.28 (c). Panel (d) is the image obtained through a Clear filter on 2013 November 30.21, already displayed in Figure 4(d), but shown here again for clarity. These images are those used in the modeling procedure. In all panels, north is up, and east is to the left.

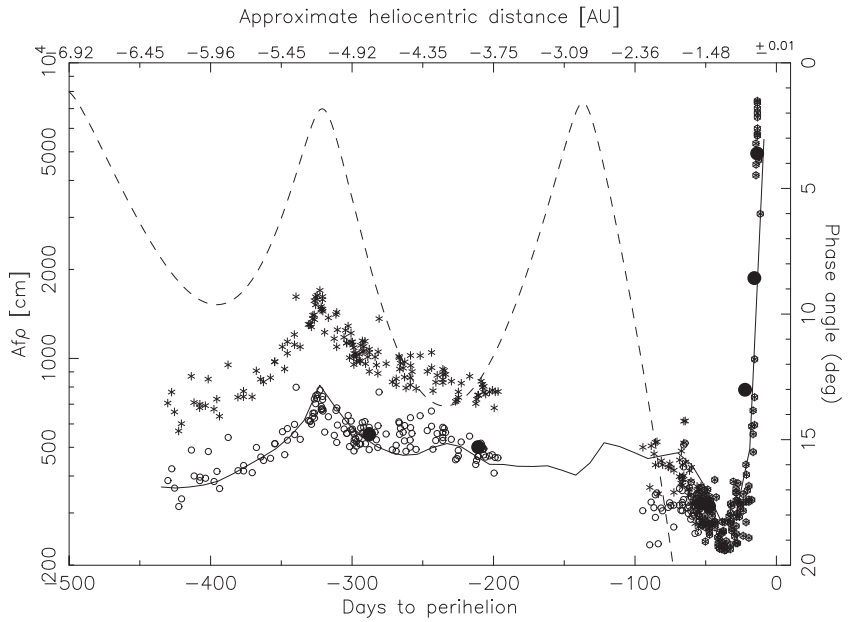

Figure 6. Original Afρ measurements by the amateur astronomical Association *Cometas-Obs* (asterisks), as a function of the heliocentric distance and time to perihelion. The open circles are the same data but corrected by the factor $10^{\kappa(30-\alpha)/2.5}$, with $\kappa = 0.03$ mag deg^{-1} for phase angles $\alpha \leqslant 30^{\circ}$ (see the text). The phase angle of the comet is displayed as a dashed line referring to the right ordinate axis. The large solid circles are the Afρ measurements obtained for the images shown in Table 1. The solid line is the modeled Afρ from synthetic images generated every 10 days for the best-fit model parameters.

data, except the *SOHO* images. These images were fitted in the last phase of the fitting procedure, since they required a special treatment, as other processes such as particle vaporization are taking place at those dates very close to perihelion.

The synthetic Afρ data were generated by computing synthetic images evenly spaced every ∼10 days with the model input parameters, and calculating Afρ at $\rho = 10^4$ km from those images. Not surprisingly, the first model results were very far from the real data set, needing corrections in several parameters of the model. Then a trial-and-error procedure is begun, in which we modified each of the input parameters at a time, then several at a time, until a reasonable fitting is found. Given the large amount of free parameters (many of them functions of the heliocentric distance), it is very difficult to follow a specific fitting strategy, other than first starting with the earlier data. After finding a reasonable order zero fit to the earliest data, we proceed to more recent data, by trying to modify only the time-dependent parameters between the last two epochs, so that

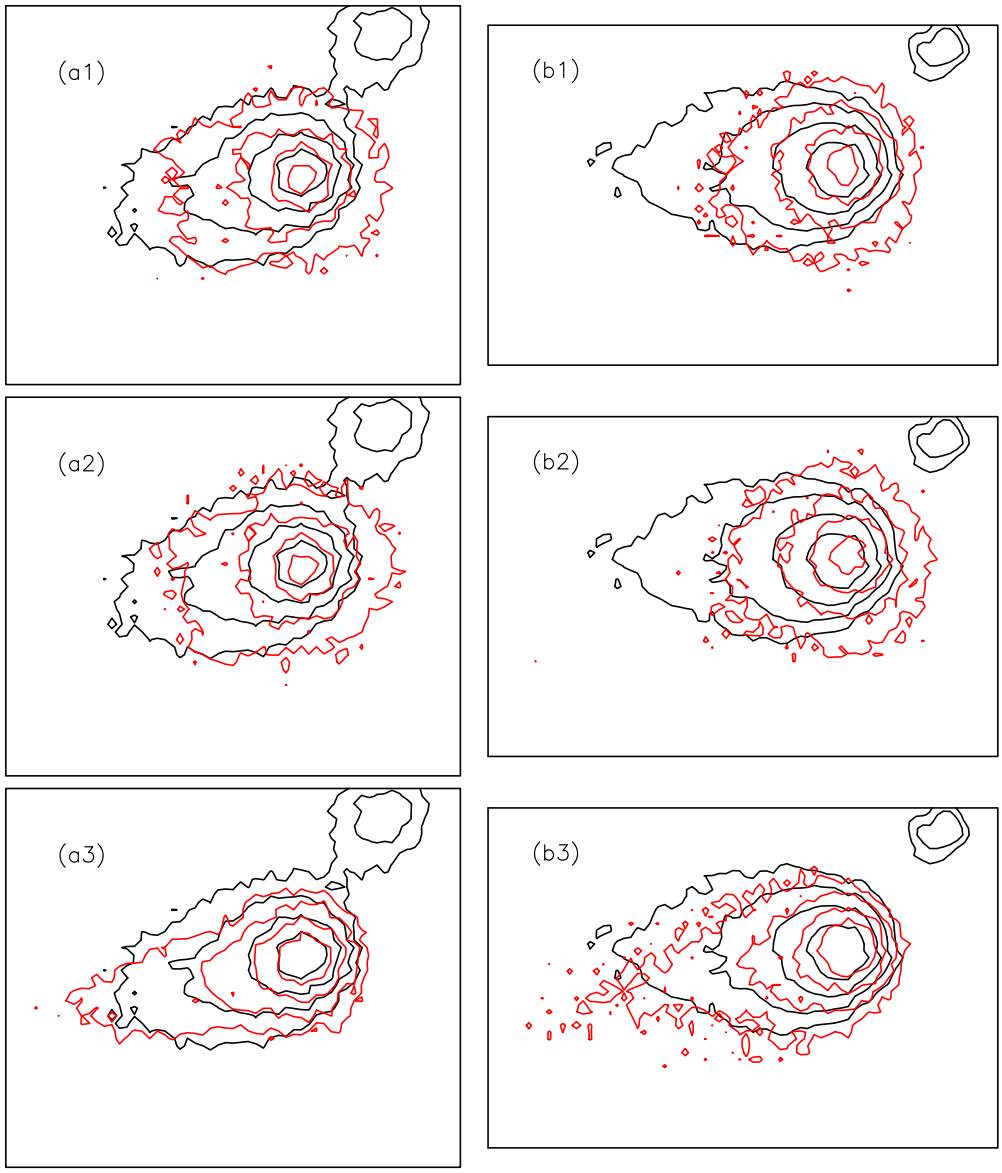

Figure 7. Observed brightness contours (black lines) and modeled contours (red lines) for the images obtained on 2013 February 14 (Panels (a1), (a2), and (a3)) and 2013 May 1 (Panels (b1), (b2), and (b3)). Panels (a1) and (b1) correspond to an isotropic ejection model. Panels (a2) and (b2) correspond to a hemispherical ejection model. Panels (a3) and (b3) correspond to a 45° emission cone toward the Sun.

(A color version of this figure is available in the online journal.)

the earlier input data are not modified. Much of the time it is impossible to find a fit to a given image without modifying earlier parameters affecting the images already fitted, so that we must go back and forth until reaching a reasonable global fit to all the data. We must recognize that the fit found is surely not unique, but taking into account the amount of data constraining the model, it is possibly the best that can be achieved with the available data.

4. RESULTS

We divided the analysis into three parts, as a function of time: the first part of data correspond to the early images and Afρ data, until approximately 200 days pre-perihelion, when the comet went behind the Sun from the Earth and could not be observed; the second part of data corresponds to those data between approximately 100 days and 13 days to perihelion, i.e., when the comet was available again to Earth's observers; and the third part corresponds to the *SOHO* data, in which the comet was $\approx\pm2$ days to perihelion. The first and second blocks of data constitute the ground-based observations and are described and analyzed in the next subsection, while the *SOHO* images and models are described in the last subsection.

The model analysis is made by first considering the simplest kind of particle ejection pattern, in which particle emission occurs within a cone of a given aperture around the vector from the comet to the Sun. This emission cone is assumed to have either a broad aperture of 90 deg (hemispherical emission), or a more focused emission of 45 deg aperture.

4.1. Ground-based Data

The first part of the data apply to the earliest images on 2013 February 14 and May 2. We first attempted to fit those images using isotropic ejection models, but those synthetic images did not accurately fit the observed images. A hemispherical ejection

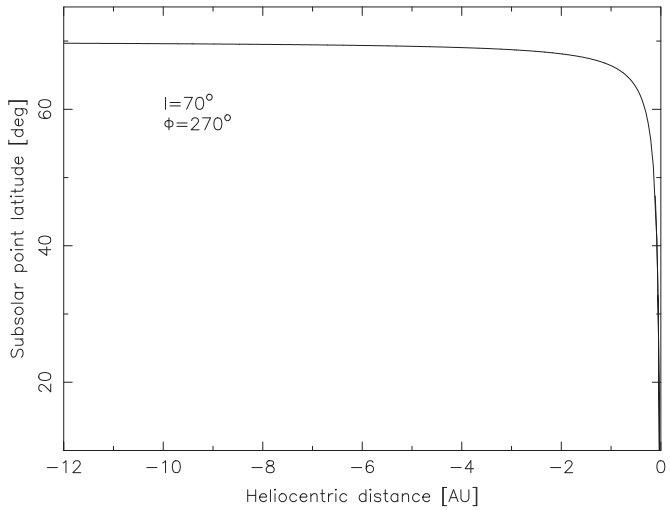

Figure 8. Variation of the latitude of the subsolar point of the comet ISON as a function of the heliocentric distance assuming a spherical nucleus with rotational axis parameters of $I = 70°$, and $\Phi = 270°$.

model (a 90 deg aperture emission cone toward the Sun) was also built up, but the results did not improve significantly. However, for narrower emission cones toward the Sun, the fits started to improve considerably. Figure 7 shows the improvement on the fits to the images from changing the emission pattern from isotropic to a 45 deg emission cone toward the Sun. In terms of a model of a rotating nucleus with an active area on it, which would be, at least conceptually, a more realistic scenario than the simple emission cone, we searched for models giving similar ejection patterns to that given by the 45 deg aperture ejection. Then, we searched in the space of parameters I, Φ, and latitude range for an active area yielding model fits of similar or better quality than those displayed in Figures 7(a3) and (b3). The best fits were found when I was near 70°, Φ close to 270°, and an active area latitude extending from 35° to 90° north. We note that the sense of rotation of the nucleus around the spin axis cannot be constrained with this model, so that this configuration would be equivalent to $I = 110°$, $\Phi = 45°$, (retrograde motion). For simplicity, we will adopt the prograde solution. The cometocentric latitude of the subsolar point, λ_{ss}, as a function of the true anomaly, θ, is given by $\sin\lambda_{ss} = \sin I \sin(\Phi + \theta)$. For $I = 70°$ and $\Phi = 270°$, λ_{ss} becomes ~70° for a large portion of the inbound branch of the comet (see Figure 8), meaning that the comet is always approximately facing the same hemisphere to the Sun inbound except for small heliocentric distances $r_h \leqslant 1$ AU, where the subsolar point changes very fast with time toward southern latitudes. The model resulting fits to the isophote field of the two images on February 14 and May 2 can be seen in Figures 9(a) and (b). These fits constitute further improvement against the simple 45 deg ejection cone. Note that the model fits must also be consistent with the evolution of the model parameters back to the onset of activity, specifically with the heliocentric variation of the Afρ curve as well. We verified that the model in fact simultaneously fits the images and the Afρ parameter as a function of time (see Figures 6 and 9) for the first part of the data, from the onset of activity to 200 days to perihelion.

The second block of data corresponds to images and Afρ data from 100 to 13 days to comet's perihelion, or from $r_h = 1.55$ to $r_h = 0.61$ AU. The application of the previously described anisotropic ejection model to those images resulted in poor fits, showing a prominent brightness excess in the sunward direction. For those images, simple isotropic ejection models performed much better, however. To satisfy both the images and Afρ data

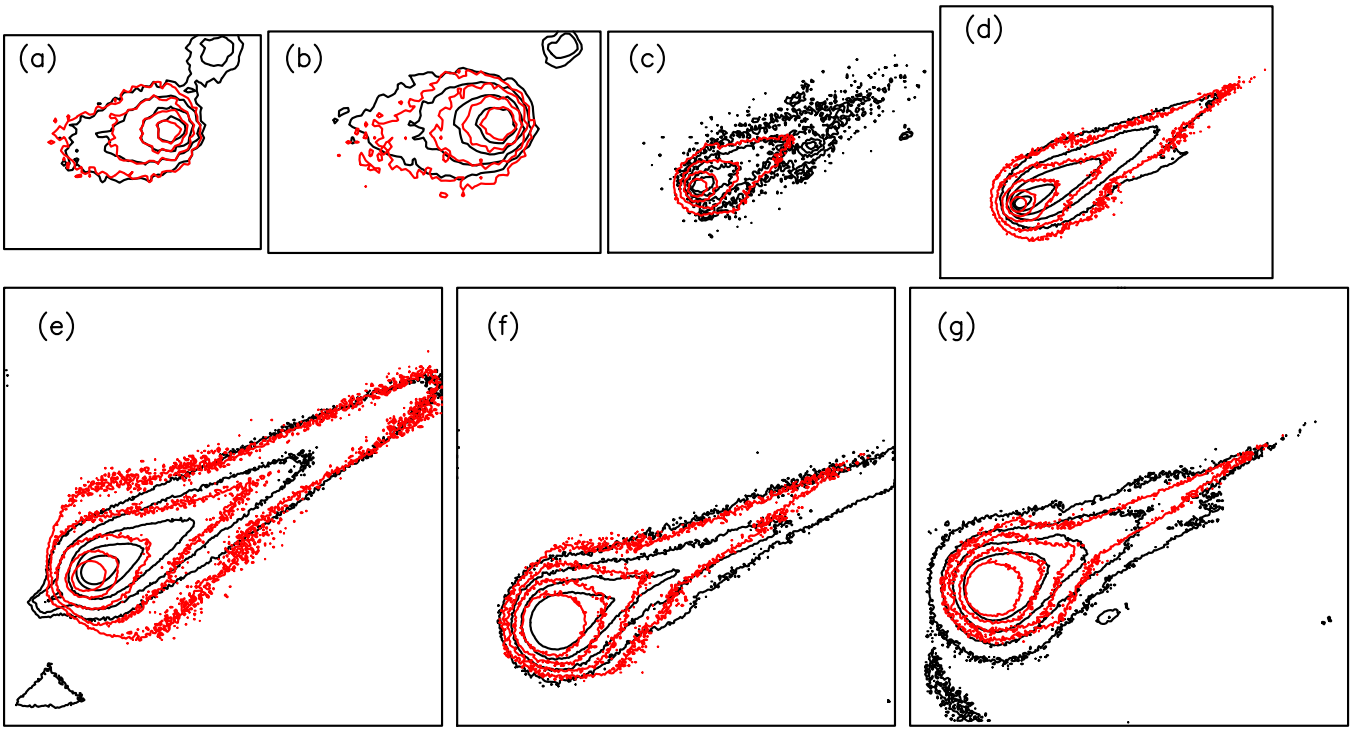

Figure 9. Observed brightness isophotes (black contours) and best-fit modeled isophotes (red contours) for the seven images labeled (a)–(g) (see Table 1 for a description of the image parameters). The best-fit model parameters are displayed in Figure 11. In all panels, north is up, and east is to the left.
(A color version of this figure is available in the online journal.)

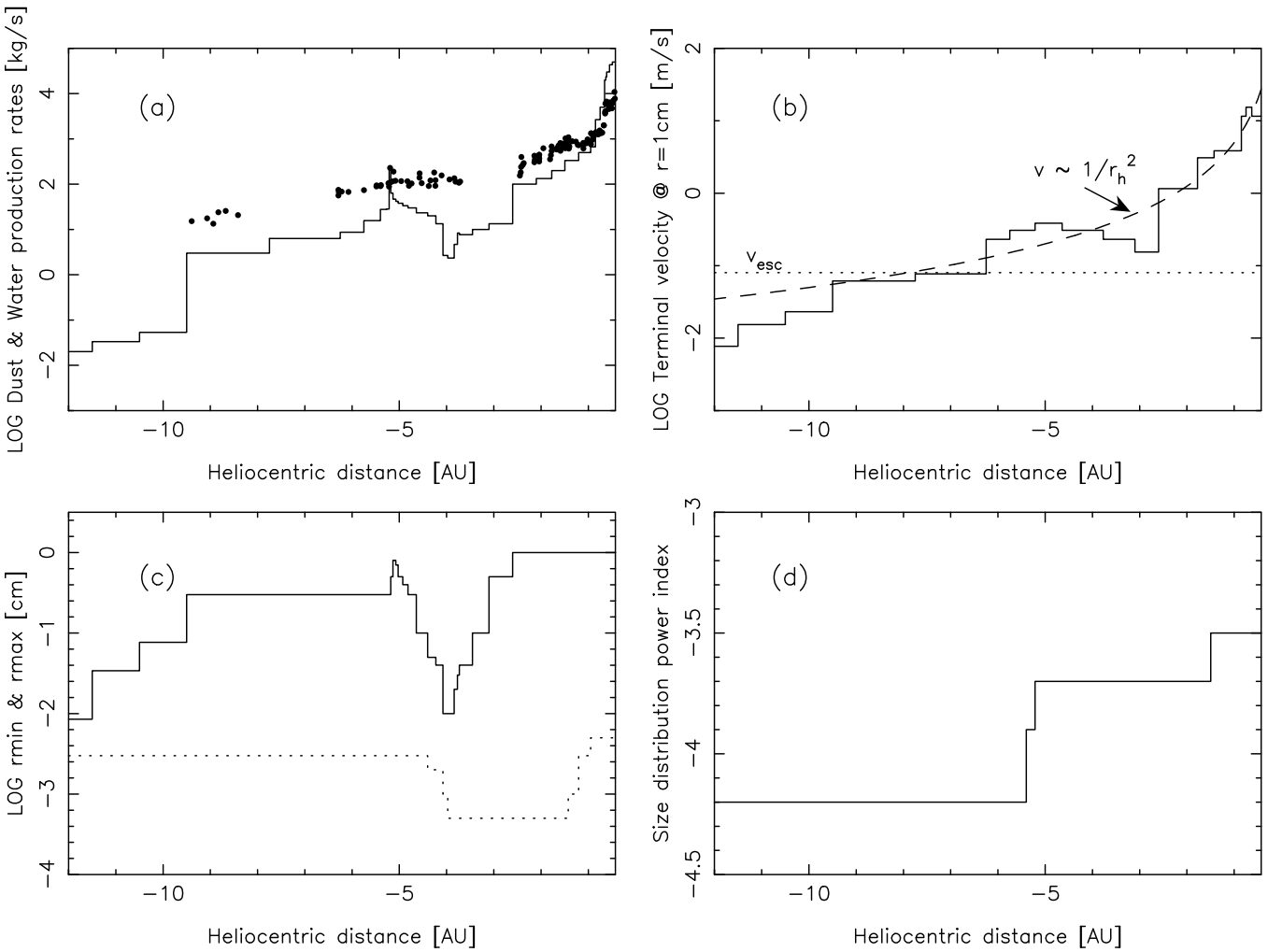

Figure 10. Best-fit parameters for the dust environment of the comet ISON. In panel (a), the dust-loss rate as a function of the heliocentric distance is shown by a solid line, while the filled circles are the water production rates calculated from the heliocentric magnitudes by the expression of Jorda et al. (2008). Panel (b) shows the variation of the ejection velocity referred to a grain of 1 cm in radius. The dashed line corresponds to a $1/r_h^2$ dependence of the velocity on r_h. The dotted line is the escape velocity assuming a spherical nucleus of radius $R_N = 500$ m and density $\rho = 1000$ kg m^{-3}. Panel (c) shows the variation of the maximum (solid line) and minimum (dotted line) grain radius as a function of the heliocentric distance. Panel (d) displays the variation of the power index of the size distribution function vs. the heliocentric distance.

for both blocks of data, we had to assume anisotropic ejection from the onset time until the May 1.86 image at $r_h = 3.89$ AU and then switch to an isotropic ejection model for heliocentric distances $r_h < 3.89$ AU. In this way, we could consistently fit all the images and the evolution of the Afρ parameter for the first and second blocks of data (Figures 6 and 9).

The large obliquity of the spin axis ($I = 70°$) agrees with the analysis of *Hubble Space Telescope* (*HST*) observations of the comet on 2013 April 10 by Li et al. (2013), who also suggests a high obliquity, in the range $I = 50°$–$80°$. Since the latitude of the subsolar point remains essentially constant until $r_h \sim 1$ AU, a potential problem of the model would be in how the emission could become isotropic for $r_h < 3.89$ AU, if only one hemisphere of the comet is continuously illuminated, and the dominating process is gas drag from sublimating ices. One possibility is the propagation of a thermal wave into the nucleus that activate subsurface sublimation in areas that previously had been inactive. Another possibility, but much more unlikely, is that the nucleus of the comet is highly elongated and has the rotating axis aligned with the long axis (i.e., in an unstable configuration because of its high energy for its angular momentum) so that very small variations in the subsolar point latitude would result in the illumination of fresh ices in the southern hemisphere, leading to sublimation.

The model parameters that best fit all available images and Afρ data are displayed in Figure 10. The dust mass-loss rate as a function of the comet heliocentric distance is displayed together with the water production rate obtained by converting the available heliocentric magnitude (m_h) data (Minor Planet Center database and N. Biver 2014, private communication) to $Q[H_2O]$ (in s^{-1}) by the expression $\log Q[H_2O] = 30.675$–$0.2453\, m_h$ (Jorda et al. 2008). In general, both quantities correlate, except for the local minimum near −4.8 AU. The dust-to-gas ratio tends to decrease with increasing heliocentric distance in general and keeps < 1 except at $|r_h| > 1$ AU. It is, however, important to note that the latest images on 2013 November 6.23, November 13.20, and, especially, November 15.24, at $r_h = 0.87$, 0.67, and 0.61 AU, respectively, are increasingly contaminated by the plasma tail, so that the dust-loss rates derived are actually an upper limit. Most of this contamination presumably comes from the H_2O^+ ion, which is the one that dominates the red region of the spectrum covered by the red bandpasses. The narrow local maximum of dust-loss rate at ∼–5.2 AU does not have a counterpart in the gas-loss rate (except for two

single magnitude estimates), and is associated to the brightness increase very likely produced by the brightness opposition effect or backscattering enhancement.

Regarding ejection velocities, as stated previously, we imposed a maximum grain size limit set by the escape velocity appropriate for an assumed 500 m radius body with a bulk density $\rho = 1000$ kg m^{-3} at a distance of 20 R_N (see the dotted line in Figure 10(b)). Then, at heliocentric distances of $|r_h| \lesssim 9$ AU, ~1 cm radius grains could in principle be ejected. However, the maximum size set at heliocentric distances $5 < |r_h| < 9$ was 0.3 cm. The reason is that the ejection of larger particles would result in the presence of a strong sunward brightness spike in the images for $|r_h| < 1$ AU, which is not observed. The grain velocities experience a strong decrease with increasing heliocentric distance, which might be approximated closely by a $1/r_h^2$ dependence (see Figure 10(b)). This agrees with the terminal subsolar velocity found by Crifo & Rodionov (1997) from advanced three-dimensional circumnuclear coma models at intermediate particle sizes, and departs from the approximate $1/r_h$ dependence stated by Whipple (1951).

The derived range of ejected grain sizes as a function of the heliocentric distance is generally constrained by the escape velocity in the upper bound. The lower size limit is constrained in combination with the power index, controlling both the absolute brightness levels of the outermost isophotes, and the variation of brightness across the tail images. The power index ranges between −4.2 at far pre-perihelion distances and −3.5 at perihelion. These are rather common values for the power index found in the literature. As an example, Fulle et al. (2010) found similar values in the post-perihelion branch in their model analysis of the dust environment of comet 67P/Churyumov-Gerasimenko.

4.2. Analysis of SOHO Images

The third block of data pertain to the previously described "level-0.5" *SOHO* fits images in both the Clear and DeepRed filters obtained with the LASCO C3 coronagraph spanning the dates around perihelion. With our Monte Carlo model we analyzed two pre-perihelion and one post-perihelion DeepRed images, and one post-perihelion Clear image. These images are described in Table 1 and are displayed in Figure 5. As stated previously, it is assumed that the DeepRed images are providing information on light scattered by dust only. The brightness observed in the pre-perihelion Clear filter images is mostly attributed to sodium emission (e.g., Knight & Battams 2014). As stated in Section 2, alkali atoms should be expected to be extracted from dust, where up to five possible mechanisms have been identified (Fulle et al. 2013), including thermal- and/or photon-stimulated desorption, solar wind sputtering, vaporization, and photodissociation of parent molecules. In consequence, the pre-perihelion Clear filter images can trace the dust grains, but their analysis should obviously take into account the emission mechanism(s) involved, and this is beyond the scope of the paper. We will only use those Clear filter pre-perihelion images to compare with the dust features observed in the DeepRed images pre-perihelion.

The choice of the LASCO C3 images analyzed was not arbitrary: we selected Clear and DeepRed images taken as close in time as possible in order to compare the observed dust features at each epoch. The first images selected correspond to 2013 November 28.02 (Clear) and 28.07 (DeepRed). At that time, the Clear filter image shows nearly the maximum level of saturation, with an apparent magnitude near −2.0, in contrast with the apparent magnitude in the DeepRed filter of ~+2.0 (Knight & Battams 2014). The next images were selected at 2013 November 28.62 (Clear) and 28.63 (DeepRed), just before the comet head was hidden by the coronagraph. Then, we selected images at 29.26 (Clear) and 29.28 (DeepRed), just after the comet emerged from the coronagraph, and yet another one when the comet was headed toward the edge of LASCO C3 field of view, but still retaining some significant signal on the Clear filter on November 30.21. At that time, no DeepRed images were available. However, and since the fluxes in the Clear and DeepRed images were similar since November 29.0 onward (Knight & Battams 2014), we assumed in principle that the flux in the Clear filter at that time (November 30.21) is given information on light scattered by dust, as in the DeepRed images, and that the alkali emission is negligible.

The analysis of the *SOHO* images is complicated by the fact that particle sublimation, among other processes, is surely playing a role. Our approach consist in fitting the tails as if they were generated in some interval of time where dust is being produced according to a set of model input parameters, but without taking into account that in the very same interval there is an unspecified fraction of particles that surely undergo variations in size, or even disappear because of sublimation. As a consequence, our estimates of the mass of particles contained in a dust tail for these *SOHO* images are always lower limits to the real dust mass ejected. For these fits, and for lack of better information, we assumed the same ejection velocity law as for the gas drag in the previous analysis. The dust ejection was assumed in principle to be isotropic.

We started the analysis with the DeepRed image on 2013 November 28.07. The close Clear filter image on November 28.02 is becoming saturated near the head of the comet, reaching approximately maximum brightness (Figure 4). The parameters of the best fit to the DeepRed image, as well as for the other *SOHO* images are shown in Figures 11 (pre-perihelion) and 12 (post-perihelion). The most remarkable feature of the fit is the large amount of dust mass needed to fit the tail, which is 2.3×10^{11} kg, equivalent to a sphere of 380 m in radius with density 1000 kg m^{-3}. This is a very significant dust mass, nearly half of that of a 500 m nucleus with $\rho = 1000$ kg m^{-3} (5.2×10^{11} kg). This is much larger than the total dust mass ejected from the onset time until the observation time of our last ground-based image on November 15.24, 7.3×10^9 kg, when the comet was at 0.61 AU. The start of the significant mass loss is at $r_h = 0.36$ AU pre-perihelion, where, after a short maximum burst, the activity continues at a high rate of 1.7×10^5 kg s^{-1}, until the observation date, November 28.07. The minimum particle sizes are rather small, ranging from about 1 μm to 0.1 μm during the peak activity, with the largest particles being ejected at ~10 m s^{-1}. The best fit image is shown in Figure 13(a), and a scan along the tail is compared to the observation in Figure 14(a). It must be noted that this strong production of particulate material at 0.36–0.08 AU is also accompanied by a strong reduction in the dust production rate at $r_h > 0.61$ AU in comparison with the derived loss rates from ground-based data at those heliocentric distances (see Figure 10(a)). Specifically, we must impose a reduction factor of at least 40 at $r_h > 0.61$ AU, otherwise the spike, which appears clearly in the northern branch of the tail in the Clear filter images (see Figure 4(a)), would appear markedly in these synthetic DeepRed images, contrary to the observations. An explanation of this on the light of particle sublimation is given in Section 4.2.1.

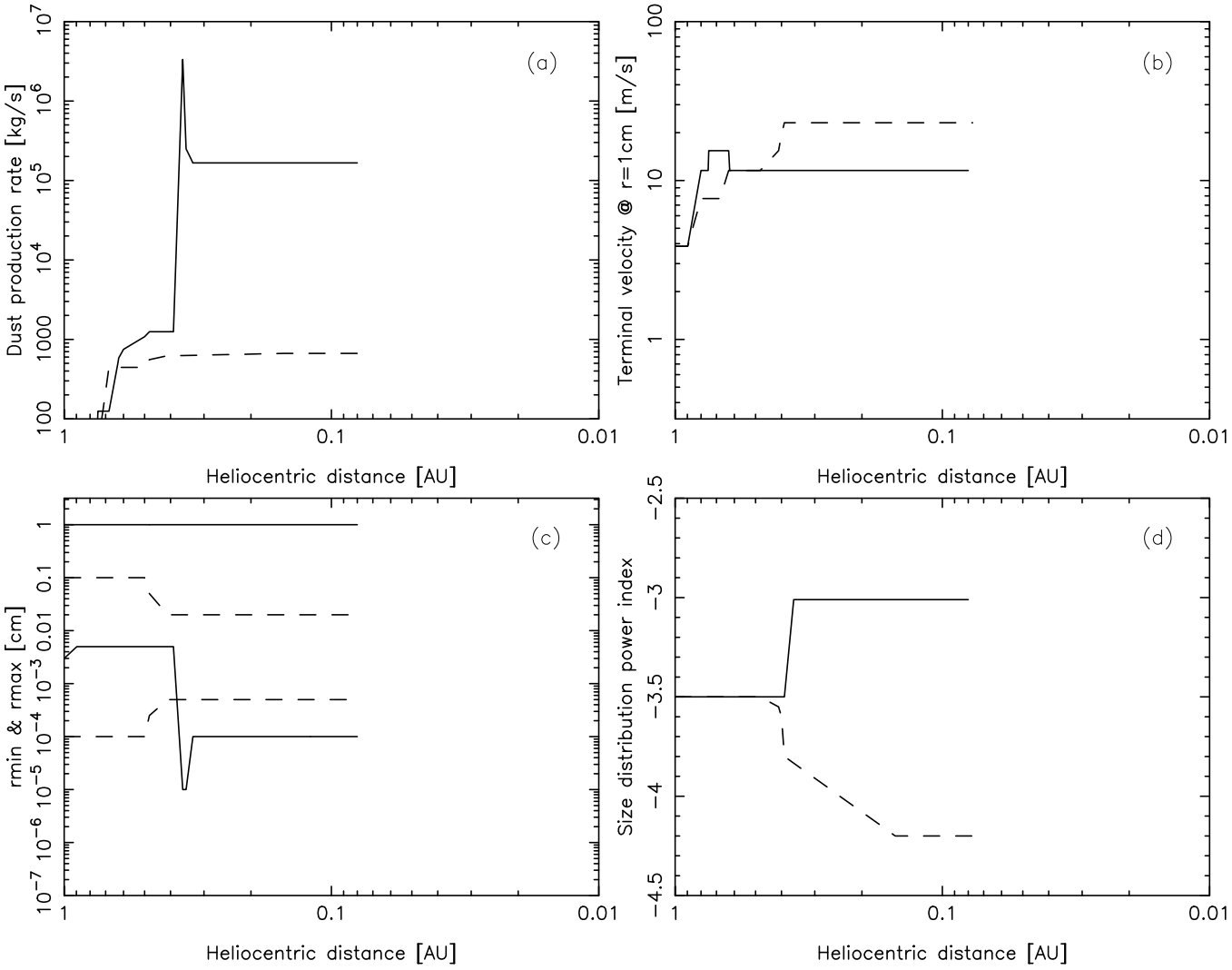

Figure 11. Pre-perihelion dust environment of the comet ISON from the selected DeepRed *SOHO* LASCO C3 images on 2013 November 28.07 (solid lines) and 28.62 (dashed lines). In panel (a), the dust production rate as a function of the heliocentric distance is displayed. Panel (b) shows the variation of the ejection velocity vs. heliocentric distance referred to a grain of 1 cm in radius. In panel (c), the maximum and minimum particle radii used in the model are displayed, and, in panel (d), the evolution of the power index of the size distribution.

The next image to fit was the DeepRed image taken on 2013 November 28.62 To fit this image, a considerable decrease in mass-loss rate in comparison with the November 28.07 image must be considered. In addition, the dust production must stop just after November 28.07, otherwise the region of the comet's heat would be much brighter than observed. Also, a notable variation in the range of particle size had to be introduced, in such a way that the distribution has become much more monodisperse (see Figure 11(c)). The dust mass contained in this tail is 7.6×10^8 kg, a factor of about 300 smaller than the mass on November 28.07. The resulting fit to the image, and a scan along both the observed and modeled tails, are shown in Figures 13(b) and 14(b). As in the case of the pre-perihelion DeepRed image on November 28.07, we imposed a strong reduction in the dust production rate at heliocentric distances of $r_h > 0.61$ AU of a factor of at least 40 (Figure 11(a)), with respect to the production rate derived from ground-based data at those heliocentric distances (Figure 10(a)), for the same reason: the spike that is clearly seen in the Clear filter image (see Figure 4(b)), which corresponds to dust ejected much earlier in the orbital path, would appear clearly in the synthetic DeepRed image of November 28.62, unless this reduction is applied. The spike only appears in a high-contrast display, such as shown in Figure 13(e), when that reduction to the dust production rate is performed.

The two post-perihelion images analyzed were taken at phase angles of 121°.1 and 127°.8 on November 29.28 and 30.21, respectively. As a consequence, a correction for the forward-scattered brightness, in a similar way as we did for the early images and Afρ data for phase angles close to backscattering, must be performed. We followed the parameterization of Marcus (2007), also used by Knight et al. (2010), for an intermediate dust-to-gas ratio of 0.52. Then, to take into account the cometary phase curve, and putting the data at the brightness level of the 30° phase angle, as for the ground-based images and Afρ data, the images on November 29.28 and 30.21 are corrected by 0.50 and 0.75 mag, respectively. Both post-perihelion observations reveal a bilobed -shaped tail, with some material in between. The dust parameters of the best fits are displayed in Figure 12, while the best-fit images are compared to the observations in Figures 13(c) and (d), while scans along the images are displayed in Figures 14(c) and (d). As stated previously, the theoretical

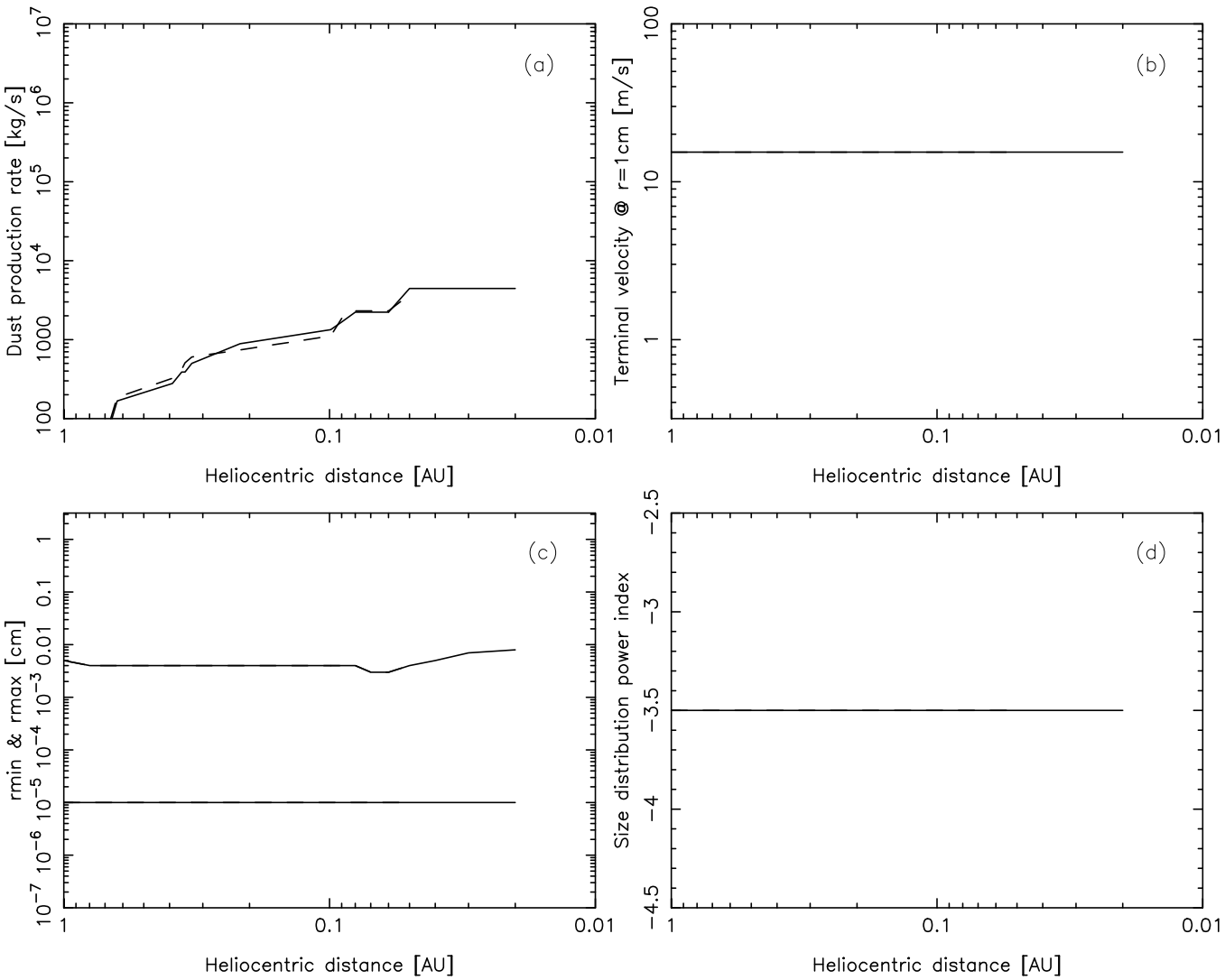

Figure 12. Post-perihelion dust environment of the comet ISON from the selected DeepRed (2013 November 29.28, solid lines) and Clear (2013 November 30.21, dashed lines) *SOHO* LASCO C3 images. In panel (a), the dust production rate as a function of the heliocentric distance is displayed. Panel (b) shows the variation of the ejection velocity vs. heliocentric distance referred to a grain of 1 cm in radius. In panel (c), the maximum and minimum particle radius used in the model are displayed, and, in panel (d), the evolution of the power index of the size distribution. Note that with the exception of panel (a), the dust environments from the analysis of both post-perihelion images are indistinguishable.

nucleus position is significantly outside the optocenter of these images. This is consistent with the fact that the comet ceases activity before perihelion, as confirmed by the model results. The dust parameters are the same for both post-perihelion images, except that the mass production stops at 0.02 AU for the November 29.28 image and at 0.05 AU for the November 30.21 image. This accounts for the difference in total dust mass released in the two observations, 8.1×10^8 kg and 6.7×10^8, respectively. It is also important to note is the very small size of the particles that constitute both tails in comparison with all previous images, being in the range 0.1–50 μm.

It must be noted that while an isotropic ejection pattern was compatible with the ejection scenario in the first of the two pre-perihelion images on November 28.07, in order to perform a good fit to the images on November 28.62, 29.28, and 30.21, an anisotropic ejection model had to be considered. Specifically, for those images (those displayed in Figures 13(b), (c), and (d)) the ejection pattern was characterized by $u_R = 0.7 + 0.3\,r_1$ and $u_\theta = 0.5 + 0.5\,r_2$ while the ejection component along the perpendicular to the orbit plane is isotropic, i.e., $u_z = 2\,r_3$–1, where r_1, r_2, and r_3 are random numbers in the (0, 1) interval. To show this, post-perihelion synthetic images built under the assumption of isotropic ejection are shown in Figure 15, where it can be seen that they not adequately reproduce the observed brightness pattern.

4.2.1. Particle Sublimation Near ISON Perihelion

To gain insight into the size variations that the particles might experience due to sublimation processes that have taken place during the ISON close approach to perihelion, we have calculated the evolution of the grain sizes for different cometary materials. We have specifically considered spherical grains of crystalline olivine, pyroxene glass, and glassy carbon as typical cometary materials. The rate of size decrease due to sublimation is governed by the Clausius–Clapeyron equation as (see, e.g., Mukai & Mukai 1973; Kimura et al. 2002)

$$\frac{dr}{dt} = -\frac{1}{\rho_p}\sqrt{\frac{M_r u}{2\pi k_B T}}\,p(T), \qquad (1)$$

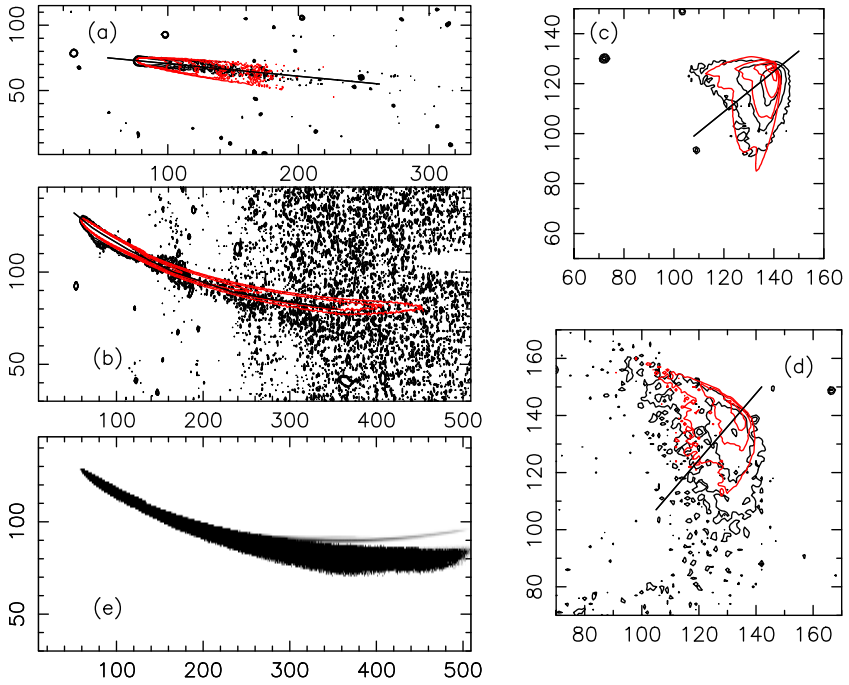

Figure 13. Panels (a)–(d): observed brightness isophotes (black contours) and modeled isophotes (red contours) for the analyzed *SOHO* LASCO C3 images. Panels (a), (b), (c), and (d) refer to the images on 2013 November 28.07, 28.63, 29.26, and 30.21, respectively (see Table 1). The black lines along the tails correspond to the brightness scans shown in Figure 14. Panel (e) shows a highly contrasted version of the model image on November 28.63 (panel (b)) intended to show the northern spike that is clearly seen in the Clear filter image (see Figure 4(b)), which is due to dust ejected much earlier in the ISON orbit.

(A color version of this figure is available in the online journal.)

where T is the temperature, ρ_p is the particle density, M_r is the molecular mass of the gas released in the sublimation process, $u = 1.66 \times 10^{-27}$ kg is the atomic mass unit, and k_B is the Boltzmann constant. The vapor pressure, $p(T)$, is given by

$$p(T) = \exp\left(-\frac{M_r u}{k_B T} L + b\right), \quad (2)$$

where L is the latent heat for sublimation, and b is a constant, which are obtained from evaporation experiments of the material involved.

The equilibrium temperature of the grains is computed from the balance between the energy absorbed and emitted using the equation (e.g., Hanner et al. 1997)

$$\frac{\pi r^2}{r_h^2} \int_0^\infty S(\lambda) Q_{\rm abs}(\lambda, r) d\lambda = 4\pi r^2 \int_0^\infty Q_{\rm abs}(\lambda, r) \pi B_\lambda(T(r)) d\lambda, \quad (3)$$

where $S(\lambda)$ is the solar flux at 1 AU, r_h is the heliocentric distance in AU, $B_\lambda(T(r))$ is the Planck function for grain temperature T, and $Q_{\rm abs}(\lambda, r)$ is the absorption efficiency of the grain of radius r at wavelength λ. The absorption efficiencies are computed for spherical grains by Mie theory, and are a function of the refractive index of the material. The refractive indices are taken from Edoh (1983) for glassy carbon, from Dorschner et al. (1995) for glassy pyroxene of composition $Mg_{0.5}Fe_{0.5}SiO_3$, and from Fabian et al. (2001), and Zeidler et al. (2011) for natural crystalline olivine in the mid-IR, and from unpublished data in the UV through the near-IR from the JENA database (http://www.astro.uni-jena.de/Laboratory/OCDB/crsilicates.html). The olivine refractive indices in the mid-IR from the three optical axes were averaged out.

The adopted values for the constants appearing in the sublimation equations are $b = 31.84$ (when MKS units are used), $L = 3.21\times10^6$ J kg^{-1}, $M_r = 169$, and $\rho_p = 3710$ kg m^{-3} for crystalline olivine, $b = 24.17$ (when MKS units are used), $L = 9.61\times10^6$ J kg^{-1}, $M_r = 60$ (see Kimura et al. 2002), and $\rho_p = 3200$ kg m^{-3} for pyroxene, and $b = 32.8$ (when MKS units are used), $L = 6.19\times10^7$ J kg^{-1}, $M_r = 12$, and $\rho_p = 2250$ kg m^{-3} for carbon. To obtain the evolution of the grain size for the different materials, we first compute the equilibrium temperature of the grains and the rate of change of the grain radius for different heliocentric distances and grain sizes. Then, we integrate Equation (1) taking into account, at each time step, the predicted heliocentric position of the comet ISON. Thus, the evolution of the grain size as a function of the heliocentric distance, for different initial grain radii and the three different compositions, is displayed in Figure 16.

The first immediate conclusion that can be drawn from Figure 16 is that grains of sizes $r \lesssim 10$ μm and of any of the studied compositions cannot survive ISON perihelion passage. In particular, crystalline olivine grains of any size will be completely vaporized at $r_h \leqslant 5$ $R_\odot$, so that grains of this composition will not survive. In contrast, pyroxene grains of sizes $r \gtrsim 100$ μm will survive, with some size reduction. Micrometer and submicrometer pyroxene grains will start to vaporize at $r_h \lesssim 10$ $R_\odot$. On the other hand, glassy carbon grains last longer than grains of the other substances, those of $r \lesssim 10$ μm being vaporized very close to perihelion, and those having $r \gtrsim 100$ μm surviving the perihelion passage with some size reduction.

From the pre-perihelion LASCO C3 image on November 28.07, we have inferred a large mass-loss rate in the 0.36–0.08 AU heliocentric distance range. Based on the extraordinary amount of dust mass contained in the tail, of

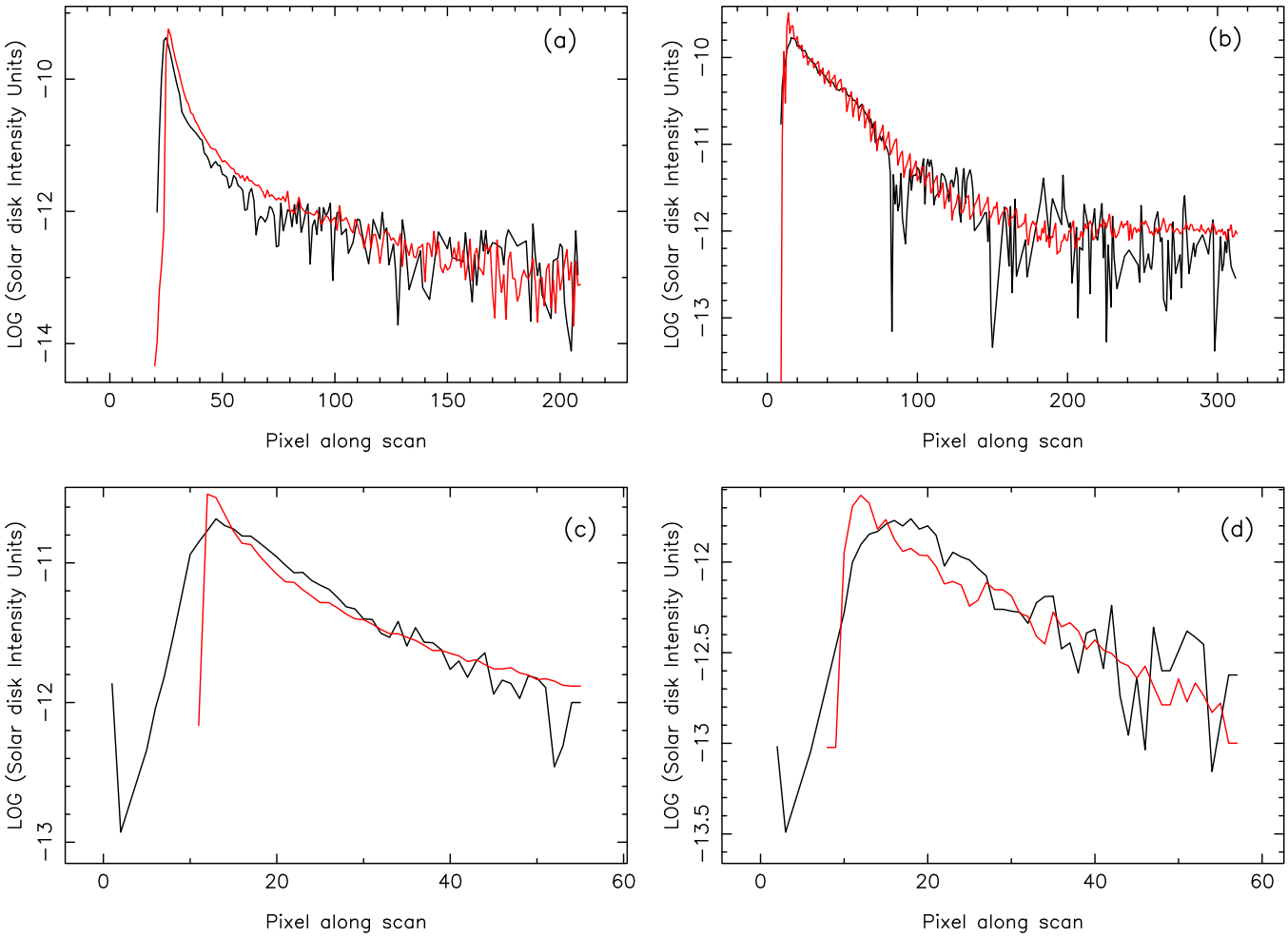

Figure 14. Brightness scans along the *SOHO* LASCO C3 images displayed in Figure 13. The black scans correspond to the observation, and the red scans to the model.

(A color version of this figure is available in the online journal.)

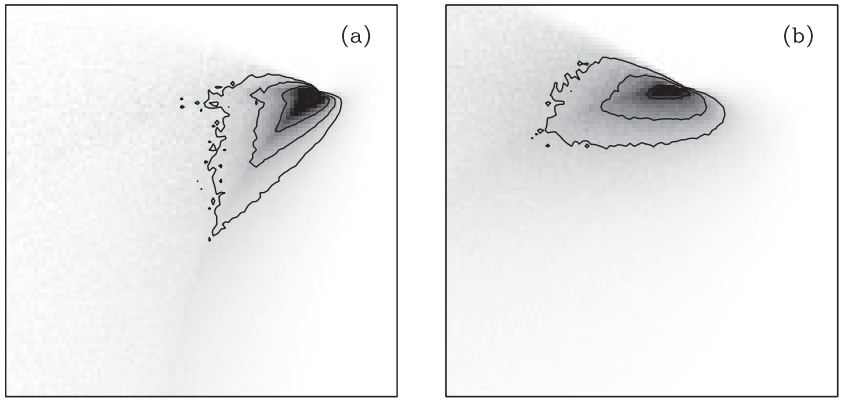

Figure 15. Synthetic images of ISON on 2013 November 29.28 (a) and 30.21 (b) under the assumption of isotropic emission.

2.3×10^{11} kg, we believe that most of the mass released is a consequence of a cataclysmic disruption of the nucleus, from whose interior a large amount of fresh material was released in the form of both ice and refractory material. This huge release of material is simultaneously accompanied by a reduction in dust production rate by a factor of at least 40 of that derived from ground-based data at $r_h > 0.61$ AU, otherwise the spike seen in the Clear filter images would show up markedly in the synthetic DeepRed image. The reason that strong reduction must be linked to the fact that the entire tail is within the LASCO C3 field of view, i.e., inside 32 solar radii or ~0.15 AU, so that particle sublimation has surely taken place (see Figure 16). During this strong ejection of material, it is interesting to note the narrow spike in dust production near 0.37 AU or 80 $R_\odot$, heliocentric distance at which the blackbody temperature is about 450 K, which is the sublimation temperature of most organics

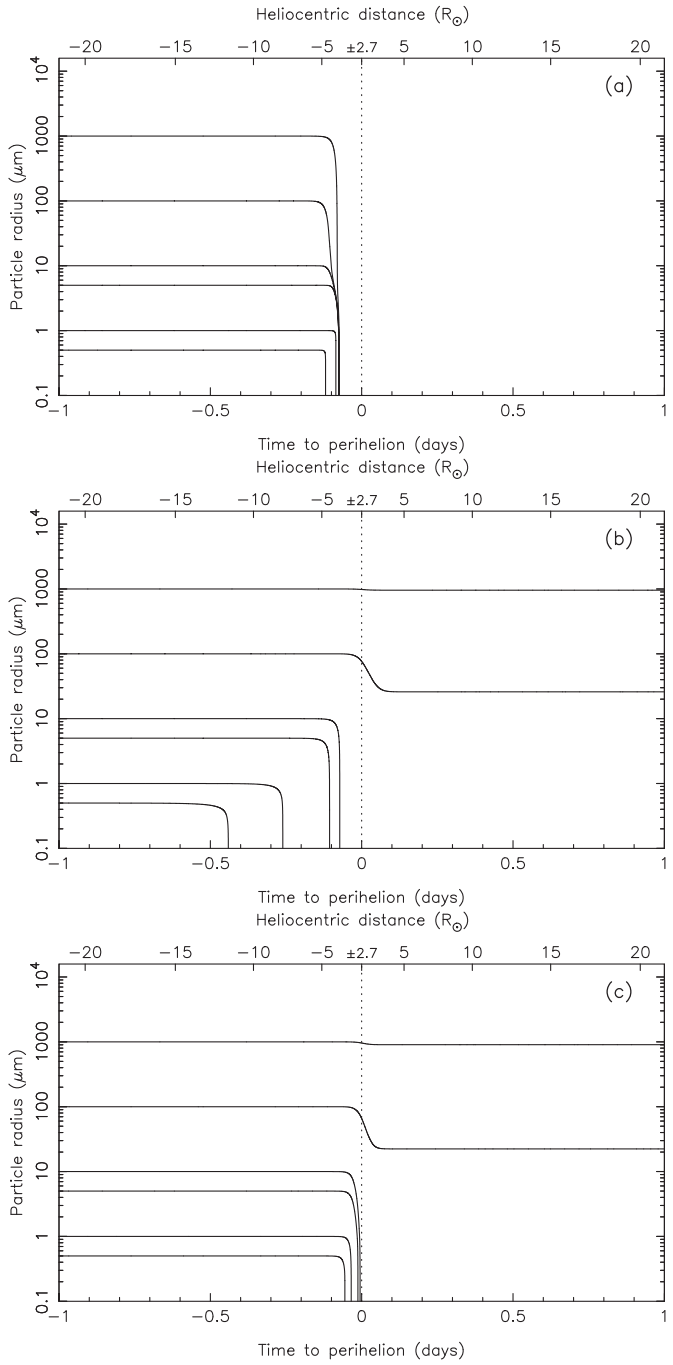

Figure 16. Evolution of grain size as a function of ISON heliocentric distance, for several initial radii and different materials: (a) crystalline olivine, (b) glassy pyroxene, and (c) carbon. For the source of the optical and sublimation constants for the different substances, see the text.

(Kouchi et al. 2002; Kimura et al. 2002). Then, if the equilibrium temperature of the grains is close to that of a blackbody, sublimation of the organic mantle covering the particles possibly takes place (Kimura et al. 2002). While the position of the spike corresponds to the heliocentric distance at which sublimation of organic compounds is expected, we cannot prove this solely from this data set.

Most of the large amount of material released in the 0.36 to 0.08 AU range is rapidly vaporized afterward as confirmed by the analysis of the November 28.62 DeepRed image, implying a strong reduction in dust mass production, mainly inward of 0.36 AU, as particle vaporization should be stronger for shorter heliocentric distances (see Figure 16). However, the total dust mass in the first post-perihelion tail on November 29.28 is approximately the same as in the post-perihelion November 28.62 tail. This would indicate that the dominant process in that time interval should be particle fragmentation, and not particle vaporization, in order to make mass conservation compatible with a decrease in grain size. It is possible that the smallest grains have undergone vaporization at distances $r_h \leqslant 5\ R_\odot$, and then the larger particles, which are essentially not vaporized, are suffering mostly fragmentation phenomena. This is consistent with the non-detection of ionized oxygen from the *Solar Dynamics Observatory* (Pesnell 2013).

Finally, the dust production rate profile corresponding to the last image analyzed on November 30.21 (the dashed line in Figure 12(a) stops at 0.05 AU (or 10.8 $R_\odot$), indicating that the material that makes the November 29.28 tail in the region 0.05–0.02 AU has been completely vaporized after undergoing the fragmentation phenomena.

5. CONCLUSIONS

We have performed a complete study of the dust environment evolution of the comet ISON by analyzing a series of images and Afρ data, spanning a period from after discovery until its almost complete vaporization a few days after perihelion. We use a Monte Carlo model to retrieve the dust parameters as a function of the heliocentric distance. The most important conclusions follow below.

The early Afρ and image data are consistent with ejection from an active area from a comet nucleus whose spinning axis has a large obliquity ($I = 70^\circ$), in agreement with the interpretation of *HST* observations of the comet by Li et al. (2013). The argument of the subsolar meridian at perihelion is found to be around ($\Phi = 270^\circ$; assuming prograde motion), and the nucleus would present a single and extended active area from 35° to 90° north. This configuration nicely fits the early images and Afρ data until approximately 200 days pre-perihelion, where the emission should vary from the mentioned active area on the northern hemisphere to become essentially isotropic afterward. The reason for that is unclear, although a plausible explanation is the propagation of a thermal wave into the nucleus that activate subsurface sublimation in areas that previously had been inactive.

The early Afρ data show a local maximum at approximately 350 days pre-perihelion which has been found to be coincident with a minimum phase angle of about 2°, showing the presence of backscattering enhancement, which has been corrected by a linear phase coefficient of $\kappa = 0.03$ mag deg^{-1}. However, a residual maximum still remains, even considering a larger κ. As a consequence, a coincidental outburst of activity cannot be ruled out.

The isotropic ejection model from approximately 200 days to perihelion to 13 days to perihelion is capable of fitting all the images and Afρ data in this interval, perfectly mimicking the minimum in the Afρ data found observationally 60 days before perihelion and the strong rise afterward. Comparing to the water production rate, we found a dust-to-gas ratio that generally decreases with increasing heliocentric distance, and a velocity ejection law that is close to a $1/r_h^2$ dependence.

The analysis of *SOHO* LASCO C3 2013 November 28.07 DeepRed images reveals that, assuming an initial nucleus of

$R_N = 500$ m with $\rho = 1000$ kg m^{-3}, at least half of the mass of the nucleus was vaporized when the comet was at about 17 $R_\odot$. At this time, based on the particle sublimation curves for different cometary materials, we conclude that the nucleus must have suffered a cataclysmic fragmentation releasing a large amount of material. The analysis of yet another pre-perihelion image on November 28.62 reveals that most of the material released was immediately vaporized after the catastrophic event, so that the nucleus itself probably disappeared at that time. The analysis of a post-perihelion LASCO C3 DeepRed image on November 29.28 reveals that the total mass has not changed with respect to the pre-perihelion November 28.62 image, while the particle size has decreased notably, which is compatible with fragmentation phenomena of the largest particles, but not with vaporization. In fact, for two analyzed compositions, pyroxene glass, and glassy carbon, particles of the size $r > 10$ μm could have survived ISON perihelion passage, experiencing only a small variation in size.

The total mass contained in the last LASCO C3 post-perihelion image analyzed, the surviving ISON material, is just 6.7×10^8 kg, or a sphere of 54 m in radius with a density of 1000 kg m^{-3}. This surviving dust is populated by small particles in the size range 0.1–50 μm, the final product of profuse vaporization and particle fragmentation process.

We thank an anonymous referee for the critical reviewing of the manuscript and constructive comments that helped to improve the paper.

We are grateful to Bernhard Fleck, who made the *SOHO* LASCO C3 images used in this paper available to us.

This work is partially based on observations collected at the Centro Astronómico Hispano Alemán (CAHA) at Calar Alto, operated jointly by the Max-Planck Institut für Astronomie and the Instituto de Astrofísica de Andalucía (CSIC), and on observations made at the 0.90 m and 1.52 m of Sierra Nevada Observatory, operated by the Instituto de Astrofísica de Andalucía (CSIC).

This work was supported by contracts AYA2012-39691-C02-01 and AYA2011-30106-C02-01 (Ministerio de Economía y Competitividad) and FQM-4555 (Junta de Andalucía).

Facilities: OSN:1.5m, OSN:0.9m, CAO:2.2m, CAO:1.2m, SOHO

REFERENCES

Agúndez, M., Biver, N., Santos-Sanz, P., et al. 2014, A&A, 564, L2
Biver, N., Agúndez, M., Santos-Sanz, P., et al. 2013, CBET, 3711, 2
Boehnhardt, H., Tubiana, C., Oklay, N., et al. 2013, CBET, 3715, 1
Combi, M. R., Fougere, N., Mäkinen, J. T. T., et al. 2014, ApJL, 788, L7
Crifo, J. F., & Rodionov, A. V. 1997, Icar, 129, 72
Domingo, V., Fleck, B., & Poland, A. I. 1995, SoPh, 162, 1
Dorschner, J., Begemann, B., Henning, T., et al. 1995, A&A, 300, 503
Draine, B. T., & Flatau, P. J. 1994, JOSAA, 11, 1491
Edoh, O. 1983, PhD thesis, Univ. Arizona, Tucson
Fabian, D., Henning, T., Jäger, C., et al. 2001, A&A, 378, 228
Fulle, M. 1989, A&A, 217, 283
Fulle, M., Colangeli, L., Agarwal, J., et al. 2010, A&A, 522, 63
Fulle, M., Molaro, P., Buzzi, L., et al. 2013, ApJ, 771, 21
Hanner, M. S., Gehrz, R. D., Harker, D. E., et al. 1997, EM&P, 79, 247
Jorda, L. J., Crovisier, J., & Green, D. W. E. 2008, LPICo, 1405, 8046
Kimura, H., Mann, I., Biesecker, D. A., & Jessberger, E. K. 2002, Icar, 159, 529
Knight, M. M., A'Hearn, M. F., Biesecker, D. A., et al. 2010, AJ, 139, 926
Knight, M. M., & Battams, K. 2014, ApJL, 782, L37
Kouchi, A., Kudo, T., Nakano, H., et al. 2002, ApJL, 566, L121
Li, J.-Y., Kelley, M. S., Knight, M. M., et al. 2013, ApJL, 779, L3
Marcus, J. N. 2007, ICQ, 29, 39
Meech, K. J., & Jewitt, D. C. 1987, A&A, 187, 585
Moreno, F., Cabrera-Lavers, A., Vaduvescu, O., et al. 2013, ApJL, 770, L30
Moreno, F., Pozuelos, F., Aceituno, F., et al. 2012, ApJ, 752, 136
Morrill, J. S., Korendyke, C. M., Brueckner, G. E., et al. 2006, SoPh, 233, 331
Mukai, T., & Mukai, S. 1973, PASJ, 25, 481
Nevski, V., & Novichonok, A. 2012, CBET, 3238
Opitom, C., Jehin, E., Manfroid, J., & Gillon, M. 2013, CBET, 3711, 3
Pesnell, D. 2013, ISON Observer's Workshop Follow-up Meeting, "SDO Observations of Comet ISON," Johns Hopkins Applied Physics Laboratory, 2013 December 6
Sekanina, Z. 1981, AREPS, 9, 113
Watanabe, J., Kawakita, H., Furusho, R., et al. 2003, ApJ, 585, 159
Whipple, F. 1951, ApJ, 113, 464
Wilson, J. K., Baumgardner, J., & Mendillo, M. 1998, GeoRL, 25, 225
Zeidler, S., Posch, Th., Mutschke, H., et al. 2011, A&A, 526, A68